Applied Physics A (2023) 129:48
https://doi.org/10.1007/s00339-022-06287-1

Applied Physics A
Materials Science & Processing

Exploring the influence of zinc substitution on structural, physical, magnetic, and DC resistivity properties of $Co_{0.5}Cu_{0.5}Fe_2O_4$ nano-ferrites

B. Trinadh[1,2] · J. Suresh[3,7] · A. Rama Krishna[4,7] · K. Vijaya Babu[5] · B. Vikram Babu[6,7] · P. V. S. S. S. N. Reddy[8] · B. Sathish Mohan[9] · K. Samatha[1]

Received: 14 September 2022 / Accepted: 28 November 2022

Abstract

High coercivity and saturation magnetization are well-known properties of the hard magnetic material cobalt ferrite ($CoFe_2O_4$). There are enormous prospects for a variety of biological, electrical, and recording applications due to many of these hard magnetic properties. The studies of $Co_{0.5}Cu_{0.5-x}Zn_xFe_2O_4$ ($x=0$, 0.1, 0.2 and 0.3) samples using thermogravimetric, X-ray diffraction, scanning electron microscopy, and infrared technology are reported in this work. The biggest exothermic peaks were initially observed between 300 and 400 °C, and they were attributed to mass loss from the thermogravimetric breakdown of the nitrate and citrate content. At (111), (220), (311), (222), (400), (422), (551), and (555), X-ray powder diffraction patterns can be seen reflecting (440). It is discovered that the transmission bands fall within the range that was anticipated based on the spectra. The produced compounds are equivalent in terms of morphology and particle size, but they are somewhat aggregated as a result of interactions between magnetic nano-ferrites. Because the porosity decreases with increasing dopant concentration, the coercivity values of the synthesized samples rise with copper content. Each compound's resistance decreases as temperature rises, indicating that all samples exhibit semiconducting characteristics.

Graphical abstract

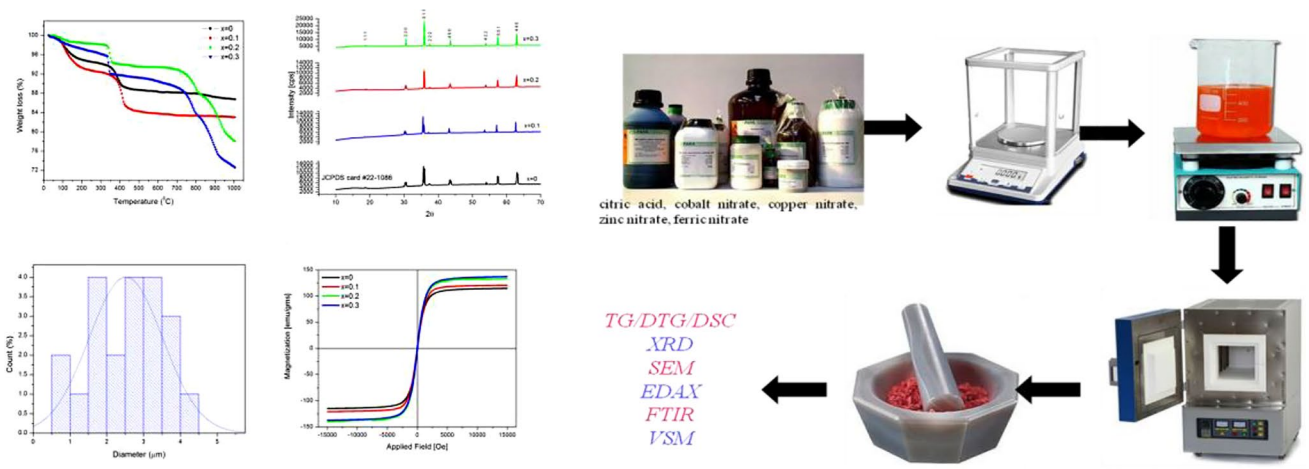

Keywords Cation distribution · X-ray diffraction · Transmission bands · Grain size · Coercivity

✉ B. Trinadh
btrinadh.vsp@gmail.com

✉ B. Sathish Mohan
bsathish401@gmail.com

Extended author information available on the last page of the article

1 Introduction

Current applications for ferrite materials include power transformers for switched mode power supply (SMPS), digital network broadband transformers, and satellite

Published online: 19 December 2022

communications [1–5]. With a distinctive crystal structure and a dark-gray or black color, ferrites are brittle, rigid, and chemically inert ceramic materials. Ferrites are highly prized, and electrical and magnetic studies are greatly influenced by their chemical composition, as well as by the many heat treatments employed in their preparation process and conditions including firing time, heating rate, cooling rate, and crystal structure. The interest in ferrites began with the search for a ferromagnetic substance with a low eddy current loss [6–9]. Because eddy current losses are proportional to resistivity, eddy current losses can be reduced by magnetic materials with greater resistivity estimates [10–12].

With the chemical formula MFe_2O_4, ferrites are ceramic magnetic materials. M stands for a metal ion that is divalent, such as iron, manganese, magnesium, nickel, zinc, cadmium, or cobalt, among others. The spinel structure that these ferrites generate is named for the mineral spinel, $CoFe_2O_4$. The main factors affecting spinel structure are the oxygen ions. Eight MFe_2O_4 molecules, thirty-two ions of oxygen, a close-packed cubic structure, and ninety-six interstitial spaces make up a spinel lattice unit cell. Among the 96 interstitial positions, there are 64 A-tetrahedral positions surrounded by 4 ions of oxygen and 32 B-octahedral positions, each surrounded by 6 ions of oxygen, in that order [12–14]. Very few of the abovementioned locations are engaged with 24 ions of metal (i.e., 8 divalent and 16 trivalent metal ions). In this work, we have synthesized $Co_{0.5}Cu_{0.5-x}Zn_xFe_2O_4$ ($x=0$, 0.1, 0.2 and 0.3) nano-ferrites using sol–gel auto-combustion route, and an assortment of characterization processes are engaged to explore the structural, physical, magnetic, and DC resistivity studies.

2 Experimental section

2.1 Materials and methodology

Using the sol–gel auto-combustion process, cobalt ferrite with the chemical formula $CoFe_2O_4$ and the copper and zinc substituted $CoFe_2O_4$ with dopant concentration $x=0$, 0.1, 0.2, and 0.3 have been produced. For this procedure, raw materials such as citric acid ($C_6H_8O_7$), cobalt nitrate ($Co(NO_3)_2.6H_2O$, 99%), copper nitrate ($Cu(NO_3)_2.3H_2O$, 98%), zinc nitrate ($Zn(NO_3)_2.6H_2O$, 99%), ferric nitrate ($Fe(NO_3)_3.9H_2O$, 99%) are used. The ratio of 1:3 between molar metal nitrates and citric acid is maintained. Ammonia solution is combined to maintain pH-7. After being sintered at 900 °C for 5 h, the powder was cooled to room temperature. A two percent PVA binder was used to granulate the sintered powder and the resulting mixes were compacted into pellets with a 10 mm diameter and 3 mm thickness. Now the pellets are subjected to sintering at 1200 °C for 5 h and subsequently cooled to normal temperature.

2.2 Materials characterization

The mass variations with heat flow were studied with TG/DTG/DSC measurements taken from HITACHI STA 7300. The manufactured structures were analyzed with PANalytical X'pert pro X-ray diffractometry (XRD) (CuKα energy with wavelength $\lambda=1.54056$ Å was used). The surface morphology and the chemical composition of the synthesized materials are studied using scanning electron microscope (SEM) and energy dispersive analysis (EDAX) on various regions by JEOL JSM-6610L. The EDAX study established the projected stoichiometric quantity of Co, Cu, Zn, and Fe ions in the currently examined sample. The IR spectra were recorded using Shimadzu spectrometer. The magnetic properties (hysteresis loop) are obtained from Lakeshore VSM instrument at room temperature. The DC resistivity analysis is carried out via Wayne-Kerr high frequency LCR meter Model 65,120 between frequencies 20 Hz-1 MHz, at temperatures between 303 and 453 K.

3 Results and discussion

3.1 DTG/TGA/DSC

The mass loss and thermal decomposition of made-up $Co_{0.5}Cu_{0.5-x}Zn_xFe_2O_4$ ($x=0$, 0.1, 0.2, and 0.3) ferrites were investigated using DTG/TGA/DSC experiments. Figure 1a–d shows the results of a thermal analysis of the manufactured samples using thermogravimetric analysis (TGA) and differential thermogravimetric analysis (DTG). The mass loss brought on by the decomposition of nitrate and citrate is what is responsible for the substantial exothermic peaks that have been observed at temperatures between 300 and 400 °C. A systematic fast decline of the curves in the TG pattern suggests that organic material or water content exhausts at temperatures between 30 and 400 °C, leading to crystallization at higher temperatures. Above 400 °C, the samples' mass loss is modest, proving that oxides are transformed into the ferrite spinel phase with crystal development. The synthesis of ferrite may be the cause of an extra exothermic peak that appears between 818 and 830 °C and has the lowest mass loss. Furthermore, we assume that samples were sintered above 850 °C because no mass loss was found above 830 °C. The DSC curve of $Co_{0.5}Cu_{0.5}Fe_2O_4$ is different than zinc substitution curves. It may be expected that the crystallite size is increasing with the zinc concentration on account of condensation reactions that may be accompanying heat treatment. But in view of earlier studies, we kept the current sintering temperature over 1200 °C for 5 h [15–17].

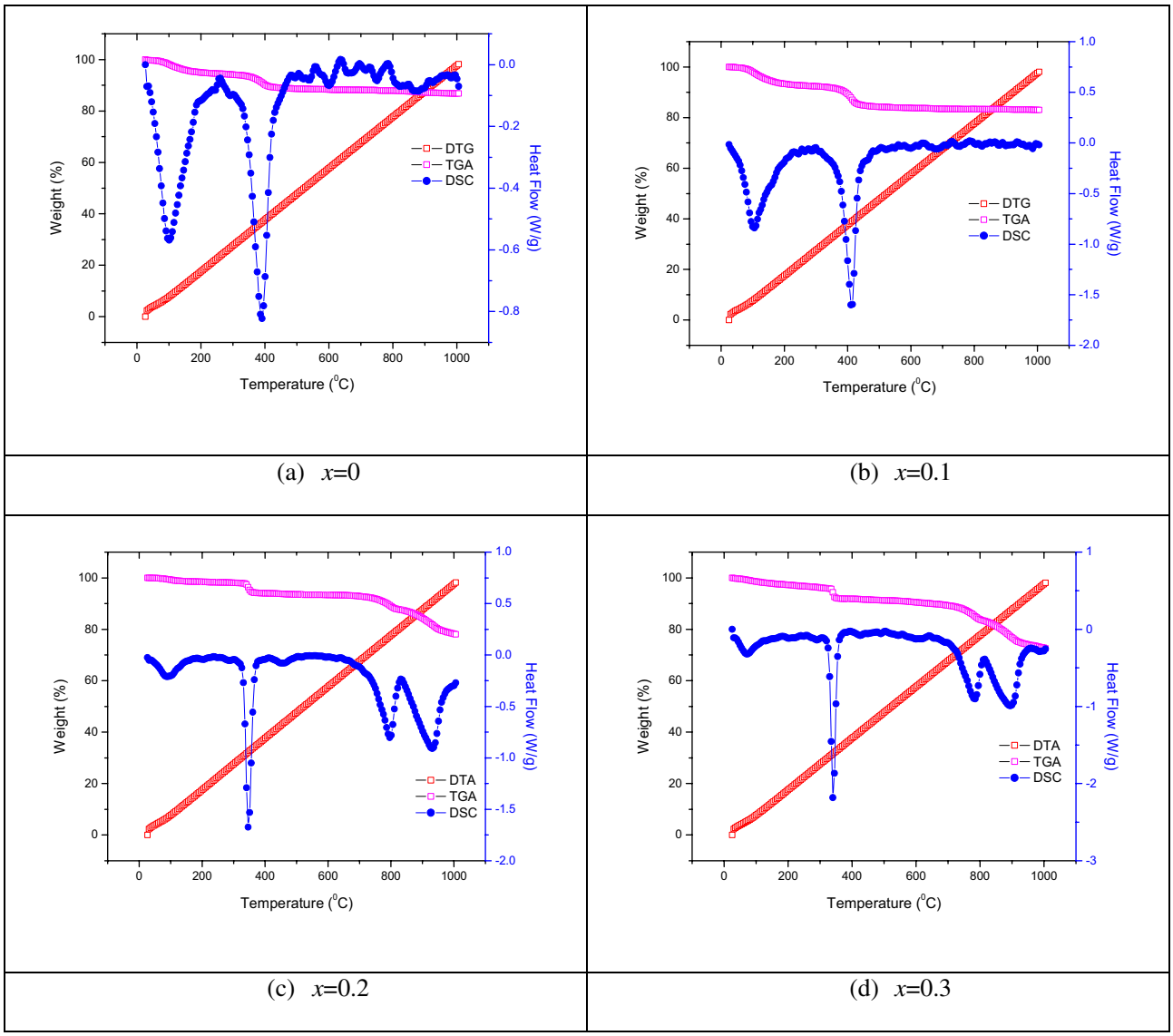

Fig. 1 TG, DTG, and DSC curves of $Co_{0.5}Cu_{0.5-x}Zn_xFe_2O_4$ ($x=0$, 0.1, 0.2, and 0.3) nano-ferrites

3.2 Structural studies

The typical variation of XRD graphs of $Co_{0.5}Cu_{0.5-x}Zn_xFe_2O_4$ ($x=0$, 0.1, 0.2 and 0.3) is shown in Fig. 2. The most significant lines of $CoFe_2O_4$ spinel ferrite sample are effectively indexed to single-phase cubic spinel structure synthesized via sol–gel auto-combustion technique which is again confirmed by JCPDS card#22-1086. The diffraction pattern peaks are matched with (2 2 0), (3 1 1), (2 2 2), (4 0 0), (4 2 2), (5 1 1), and (4 4 0) reflection planes confirming cubic spinel structure. The similar behavior is observed in $Co_{0.5}Cu_{0.5-x}Zn_xFe_2O_4$ ($x=0$, 0.1, 0.2, and 0.3) ferrite prepared with similar conditions. The parameter (*a*) is estimated taking into consideration the values of inter-planar spacing (d) and (*hkl*) indices depicted by Miller. The lattice constant (*a*) numbers are tabulated in Table 1. Cubic structure of the spinel class and single phase belonging to the Fd-3 m space group is observed in the generated nano-ferrite samples. For all the sintered compounds, XRD relieved no impurity phase. The substituted Zn^{2+} and Cu^{2+} content has a substantial effect on the relative strength and breadth of the diffracted peaks. The crystallite size of $CoFe_2O_4$ is 64 nm and this size rises for all materials. When a spinel-like structure is doped with zinc and copper ions, the elastic deformation of the material causes a homogeneous strain in the lattice. The diffraction peaks shift to a lower 2θ location as a result of this impact, changing the lattice plane spacing. Figure 3 shows the variation of lattice parameter and crystallite size with Cu composition.

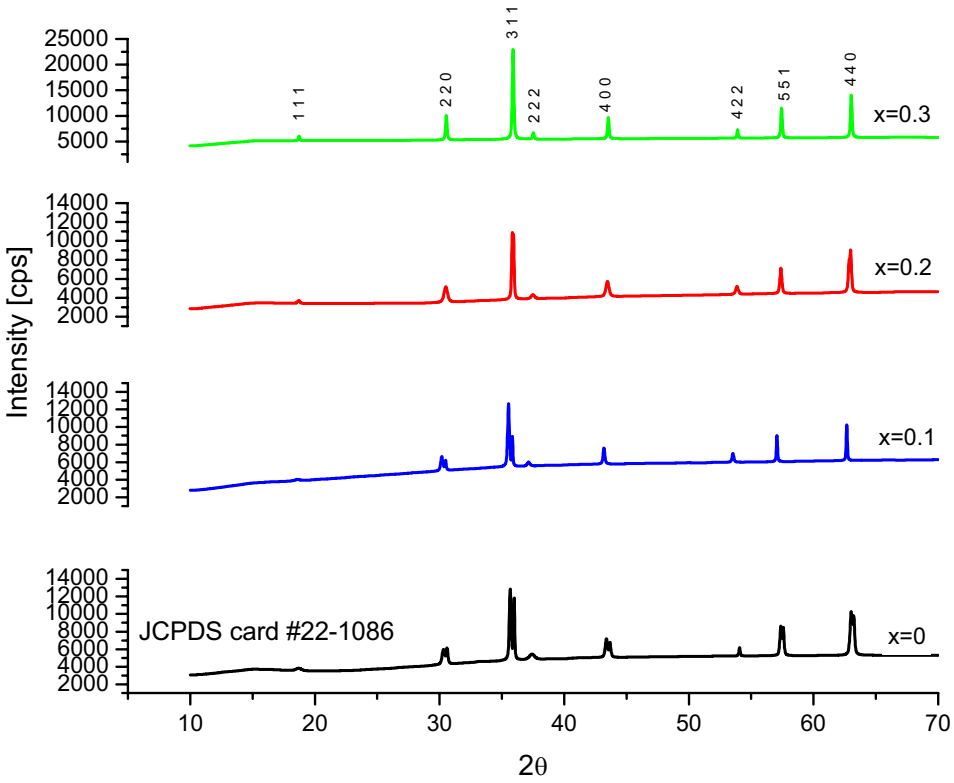

Fig. 2 XRD patterns of $Co_{0.5}Cu_{0.5-x}Zn_xFe_2O_4$ ($x=0$, 0.1, 0.2, and 0.3) nano-ferrites

Table 1 Lattice constant, crystallite size, and X-ray density of $Co_{0.5}Cu_{0.5-x}Zn_xFe_2O_4$ ($x=0$, 0.1, 0.2, and 0.3) nano-ferrites

Compound	Lattice constant (Å)	Crystallite size (nm)	X-ray density (gm/cm^3)
$Co_{0.5}Cu_{0.5}Fe_2O_4$	8.3526	64	5.4614
$Co_{0.5}Cu_{0.4}Zn_{0.1}Fe_2O_4$	8.3559	71	5.4595
$Co_{0.5}Cu_{0.3}Zn_{0.2}Fe_2O_4$	8.3567	87	5.4535
$Co_{0.5}Cu_{0.2}Zn_{0.3}Fe_2O_4$	8.3591	89	5.4458

The Cu, Zn, and Co ionic radii difference is responsible for the observed crystallite size variance. According to the literature, the lattice constant and micro strain has a similar relationship with crystallite size. The molecular weight and volume of the unit cell were used to compute the X-ray density of all produced materials. It drops from 5.4614 to 5.4458 g/cm^3. The lattice parameter is inversely related to the density of X-rays. Table 1 reveals an increase in lattice constant and a corresponding fall in X-ray density with rise in Cu ratio [17, 18].

By adjusting the equation previously described and using cation distribution, it is possible to determine the mean ionic radius of the octahedral B-site and tetrahedral A-site. The larger Cu^{2+} (0.72 Å) ions are migrating more quickly from the B-site to the A-site, replacing the smaller Fe^{3+} (0.67 Å) ions at the B-site, which causes the r_A to fall for $x=0.1$ and

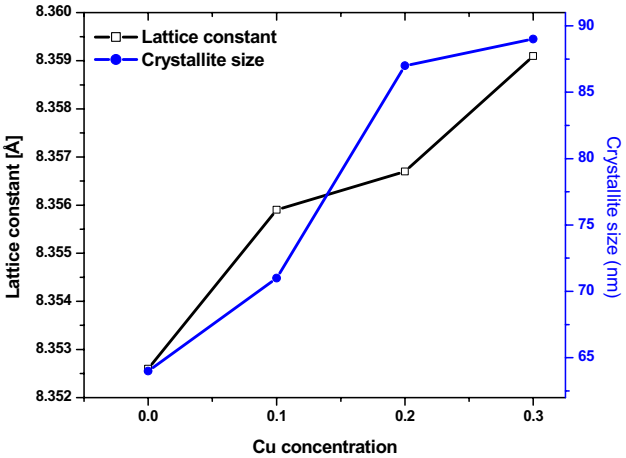

Fig. 3 Variation of lattice constant and crystallite size with Cu composition

$x=0.2$. When $x=0.3$, Cu^{2+} (0.72 Å) begins to occupy the A-site, replacing Zn^{2+} (0.83 Å) ion, which causes the r_A to increase. The gradual rise in 'r_B'($x=0.3$) results from the gradual replacement of Cu^{2+} ions at the B-sites with bigger Zn^{2+} ions. When $x=0.3$, r_B increases rapidly, which is caused by the migration of Cu^{2+}ions from the B-site to the A-site and, in turn, Zn^{2+} ions from the A-site to the B-position. Table 2 shows the list depicting radii of ions located at

Table 2 Ionic radii of tetrahedral A-site (r_A), octahedral B-site (r_B), theoretical lattice constant (a_{th}) and oxygen positional parameter (u) of $Co_{0.5}Cu_{0.5-x}Zn_xFe_2O_4$ ($x=0$, 0.1, 0.2, and 0.3)

Compound	r_A (Å)	r_B (Å)	a_{th} (Å)	u value (Å)
$Co_{0.5}Cu_{0.5}Fe_2O_4$	0.6299	0.6748	8.5075	0.3735
$Co_{0.5}Cu_{0.4}Zn_{0.1}Fe_2O_4$	0.5875	0.7870	8.5087	0.3735
$Co_{0.5}Cu_{0.3}Zn_{0.2}Fe_2O_4$	0.5744	0.7921	8.5174	0.3735
$Co_{0.5}Cu_{0.2}Zn_{0.3}Fe_2O_4$	0.5831	0.7935	8.5242	0.3735

Table 3 Cation distribution and intensity ratios of $Co_{0.5}Cu_{0.5-x}Zn_xFe_2O_4$ ($x=0$, 0.1, 0.2, and 0.3)

Material	Cation distribution	
	A-site	B-site
$Co_{0.5}Cu_{0.5}Fe_2O_4$	$(Co_{0.5}Fe_{0.7})$	$[Cu_{0.5}Fe_{1.3}]O_4$
$Co_{0.5}Cu_{0.4}Zn_{0.1}Fe_2O_4$	$(Cu_{0.2}Co_{0.5}Fe_{0.65})$	$[Cu_{0.2}Zn_{0.1}Fe_{1.35}]O_4$
$Co_{0.5}Cu_{0.3}Zn_{0.2}Fe_2O_4$	$(Cu_{0.15}Co_{0.5}Fe_{0.625})$	$[Cu_{0.15}Zn_{0.2}Fe_{1.375}]O_4$
$Co_{0.5}Cu_{0.2}Zn_{0.3}Fe_2O_4$	$(Cu_{0.1}Co_{0.5}Fe_{0.62})$	$[Cu_{0.1}Zn_{0.3}Fe_{1.38}]O_4$

the sites of tetrahedral-A (r_A), octahedral-B (r_B), theoretical lattice parameter (a_{th}), and oxygen positional parameter (u) of $Co_{0.5}Cu_{0.5-x}Zn_xFe_2O_4$ ($x=0$, 0.1, 0.2, and 0.3).

3.3 Suggested cation distribution

The examination of X-ray diffraction patterns was used to determine the cation distribution in the current system. The observed intensity ratios in this method were compared with the ratios of estimated intensities. Bertaut's research is being done now. The cation distribution is calculated using method. This technique chooses a few reflection pairs based on the statement

$$\frac{I_{hkl}^{Obs}}{I_{h'k'l'}^{Obs}} \propto \frac{I_{hkl}^{Cal}}{I_{h'k'l'}^{Cal}}$$

where I_{hkl}^{Obs} and I_{hkl}^{Cal} are the experimental seen and theoretically deliberated intensities for reflection (hkl), in that order. When matching up these ratios of intensity for reflections whose intensities (1) are almost not dependent on the oxygen parameter, (2) vary oppositely in direction with the cation, and (3) do not significantly differ, this method yields the best information on cation distribution.

The physical properties of the ferrite are principally affected by the allotment of cations between the sub-lattice A and B. The following equation is utilized to compute the cation distribution of cobalt ferrites samples using the $CoFe_2O_4$ formula,

$$\left[Co_xFe_{1-x}\right]\left[Co_{1-x}Fe_{1+x}\right]O_4$$

The tetrahedral and the octahedral positions are indicated by parenthesis and bracket respectively, x is the inverse parameter that governs the distribution of cations among the tetrahedral and octahedral locations in cobalt ferrite samples. Comparison of reflection intensities belonging to the calculated and observed data coming from plates (220), (311), (400), (422), (511), (440) yields the best data on $CoFe_2O_4$ cation distribution [18, 19, 25]. The contents of Tables 3 and 4 show that Co^{2+} ions live in tetrahedral A-site. The Zn^{2+} and Cu^{2+} ions largely restore Co^{2+} to the tetrahedral location. The suggested intensities, as well as the cation distribution are tabulated.

3.4 W–H plots

The graphs for $\beta\cos\theta$ versus $4\sin\theta$ for all the synthesized systems for ferrites are portrayed in Fig. 4. The y-intercept magnitudes and the slopes for the graphs drawn are exploited to guess the crystallite sizes and lattice strain values. The lattice parameter pertaining to the experiment was deducted by interpreting the data obtained via X-ray powder diffraction experiment by means of the 2θ numbers [18]. The increase in crystallite size reflects in the decrease of lattice strain. High level of inconsistency was seen between the experimentally reported lattice constant and the theoretically calculated number. It is argued that the secondary phases seen in the current ferrite samples may predominantly affect structural properties leading to smaller lattice parameter numbers when compared to reported values.

3.5 SEM analysis

The surface morphologies of the synthesized $Co_{0.5}Cu_{0.5-x}Zn_xFe_2O_4$ ($x=0$, 0.1, 0.2, and 0.3) samples formed at 1200 °C are shown in Fig. 5. The particles constituted of nearly spherical shape with grain sizes are 3.27 µm, 3.22 µm, 1.90 µm, and 2.56 as shown in Fig. 6. XRD measurements of average crystallite sizes of produced substances are substantially smaller than SEM measurements. This demonstrates that each particle is made up of a collection of crystallites or grains [19–21]. According to the literature, the XRD crystallite size and SEM particle size have a direct relationship, implying that a particle can be created by agglomeration of crystallites. The size of the secondary particles, which comprises several or more crystallites by soft reunion, is the size of the secondary particles observed by SEM. Furthermore, only the size of a single crystallite is revealed by X-ray line broadening analysis [22–24]. Figure 5 shows also the quantitative results of EDS analysis that is carried out on the synthesized samples. The results confirmed the presence of all the elements i.e., Zn, Fe, Co, Cu, and O ions in the synthesized samples. It is confirmed

Table 4 Intensity distribution of $Co_{0.5}Cu_{0.5-x}Zn_xFe_2O_4$ ($x=0$, 0.1, 0.2, and 0.3)

Material	$I_{(220)}/I_{(400)}$		$I_{(422)}/I_{(440)}$		$I_{(220)}/I_{(440)}$	
	Obs.	Cal.	Obs.	Cal.	Obs.	Cal.
$Co_{0.5}Cu_{0.5}Fe_2O_4$	0.9298	0.9736	0.5621	0.5005	0.5550	0.5522
$Co_{0.5}Cu_{0.4}Zn_{0.1}Fe_2O_4$	0.9164	0.9602	0.5367	0.4871	0.5416	0.5388
$Co_{0.5}Cu_{0.3}Zn_{0.2}Fe_2O_4$	0.9094	0.9532	0.5297	0.4801	0.5346	0.5318
$Co_{0.5}Cu_{0.2}Zn_{0.3}Fe_2O_4$	0.9304	0.9742	0.5507	0.5011	0.5556	0.5528

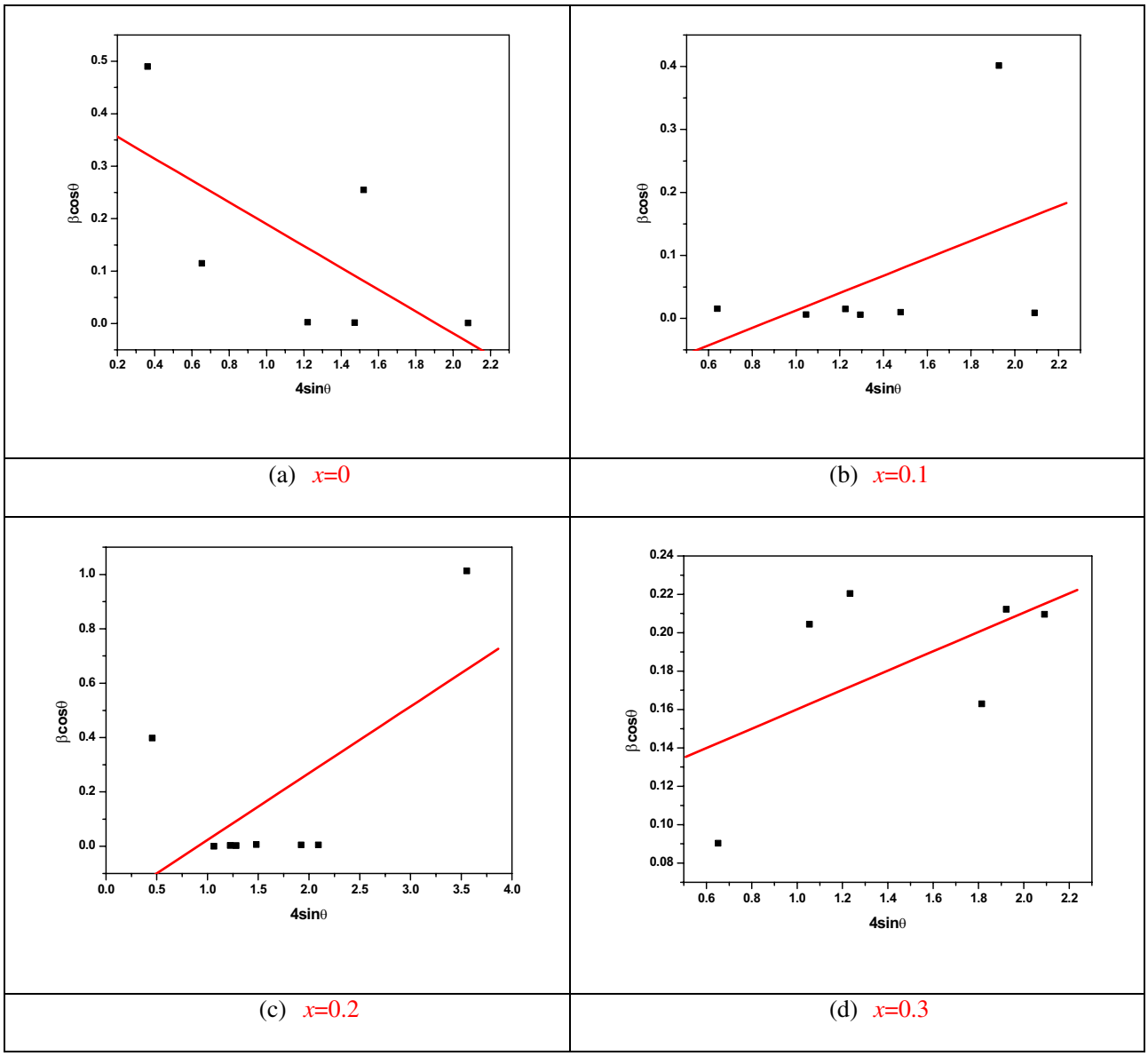

Fig. 4 W–H curves of $Co_{0.5}Cu_{0.5-x}Zn_xFe_2O_4$ ($x=0$, 0.1, 0.2, and 0.3) nano-ferrites

that the final composition of the sample is the same as that of starting composition without any impurity elements.

3.6 IR spectra

Infrared (IR) spectra of $Co_{0.5}Cu_{0.5-x}Zn_xFe_2O_4$ series nano-ferrites obtained in the range 200–1300 cm^{-1} are shown in Fig. 7. Spinel ferrites v_1 and v_2 have two distinct bands, one

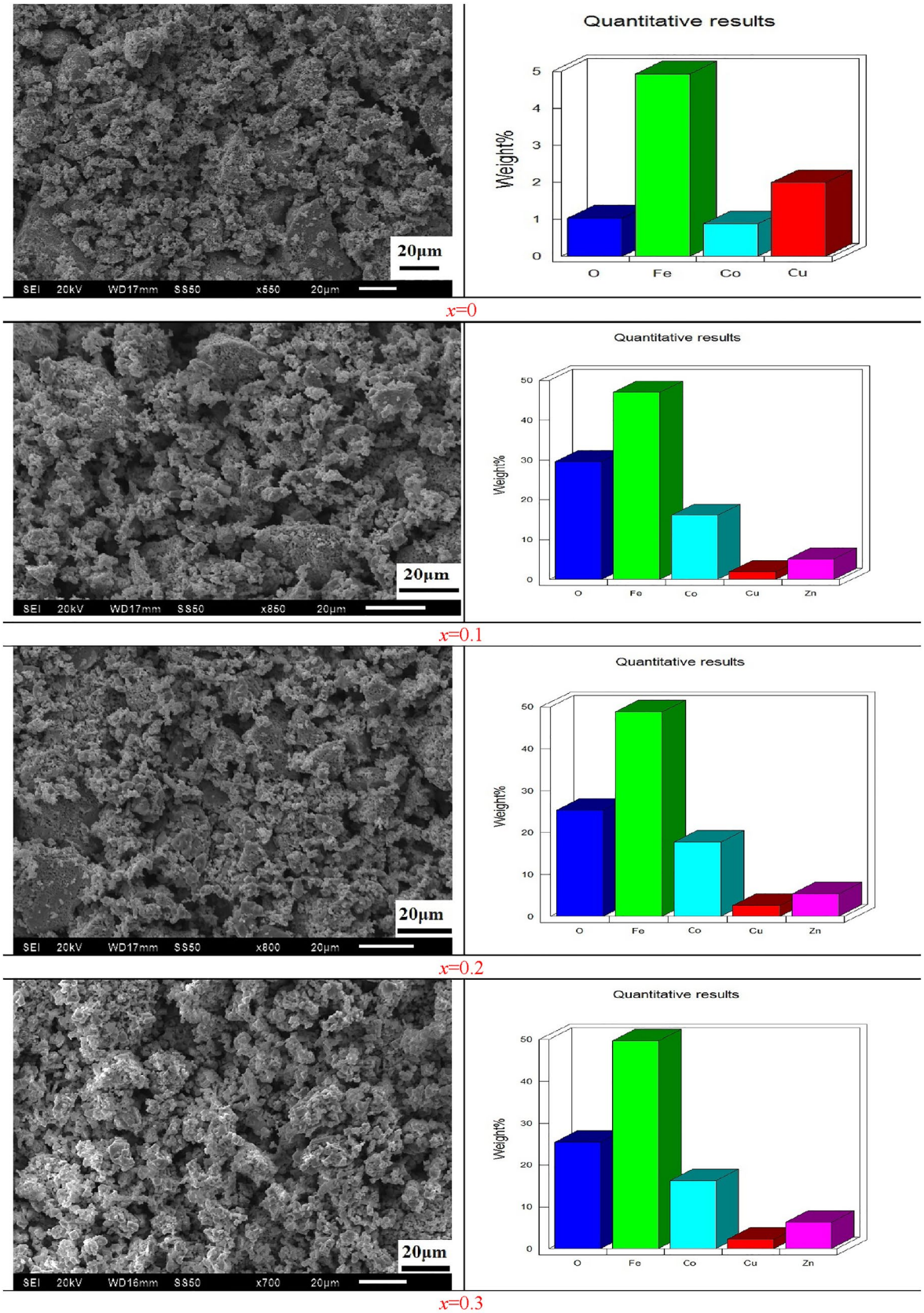

Fig. 5 SEM and EDS images of synthesized $Co_{0.5}Cu_{0.5-x}Zn_xFe_2O_4$ ($x = 0$, 0.1, 0.2, and 0.3) nano-ferrites

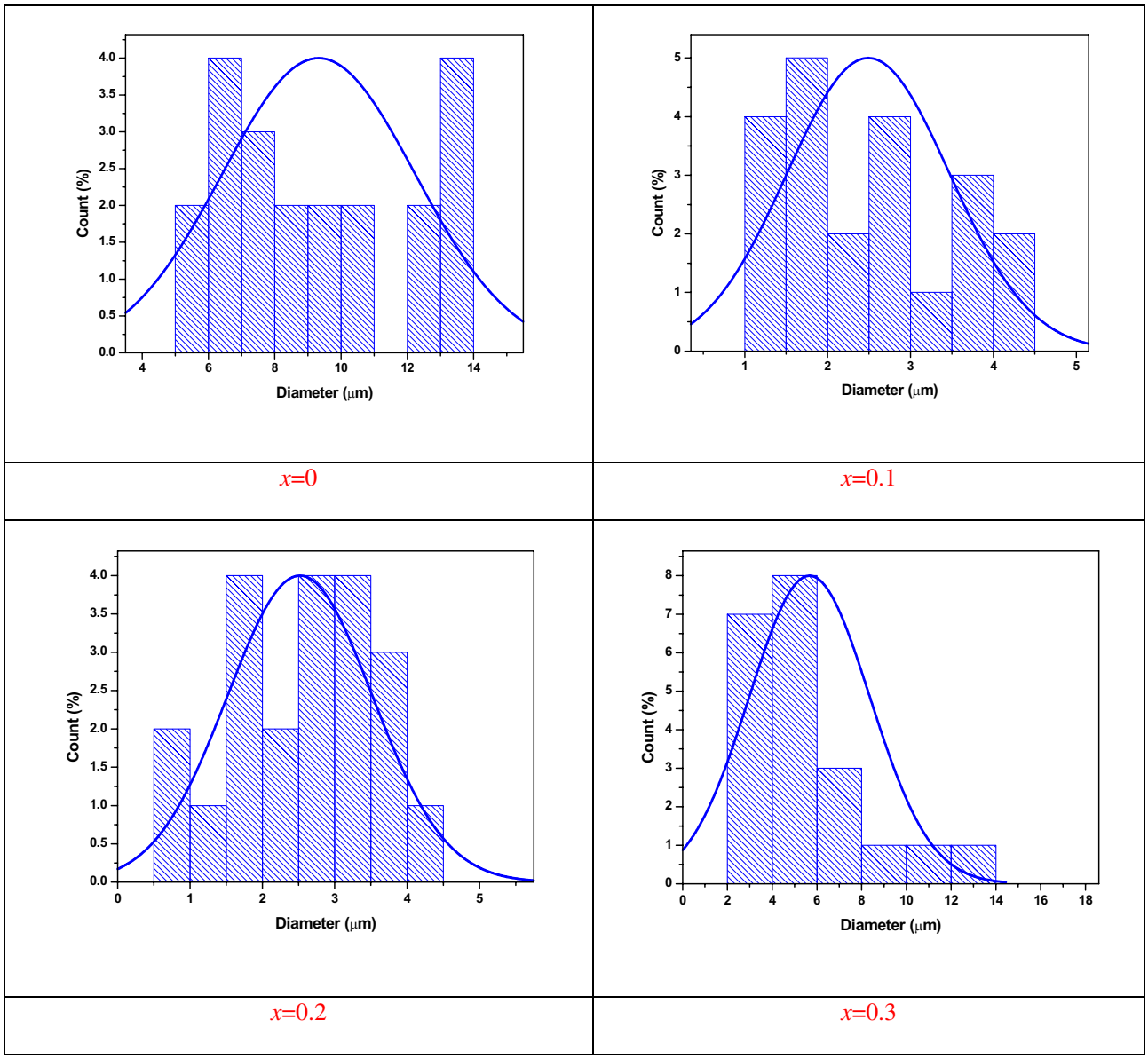

Fig. 6 Histograms of $Co_{0.5}Cu_{0.5-x}Zn_xFe_2O_4$ ($x=0$, 0.1, 0.2, and 0.3) nano-ferrites

between 574 and 582 cm^{-1} and the other between 397 and 470 cm^{-1}. The band 1 corresponds to inherent vibrations of stretching belonging to the tetrahedral A-positions metal ion–oxygen bonds, which have the maximum restoring force, while the band 2 corresponds to intrinsic bond-bending vibrations of the octahedral B-positions metal ion–oxygen complexes. The presence of absorption bands 1 and 2 in IR spectra validates the single-phase cubic spinel structure of $Co_{0.5}Cu_{0.5-x}Zn_xFe_2O_4$ ($x=0$, 0.1, 0.2, and 0.3) materials. The values of 1 are more than 2, indicating that the tetrahedral cluster's normal mode of vibration is greater in comparison to the octahedral bunch. This is endorsed to the smaller A-location bond length in comparison with the B-position ones [25, 26].

3.7 Magnetic properties

The vibrating sample magnetometer is used for reorganization of magnetic properties of the synthesized ferrites at room temperature and is shown in Fig. 8. From the obtained data, we can determine saturation magnetization (M_s), remnant magnetization (M_r), and coercivity (H_c). The saturation magnetization values, remnant magnetization values, and coercivity values of $Co_{0.5}Cu_{0.5-x}Zn_xFe_2O_4$ ($x=0$, 0.1, 0.2, and 0.3) nano-ferrites are listed in Table 5. From these

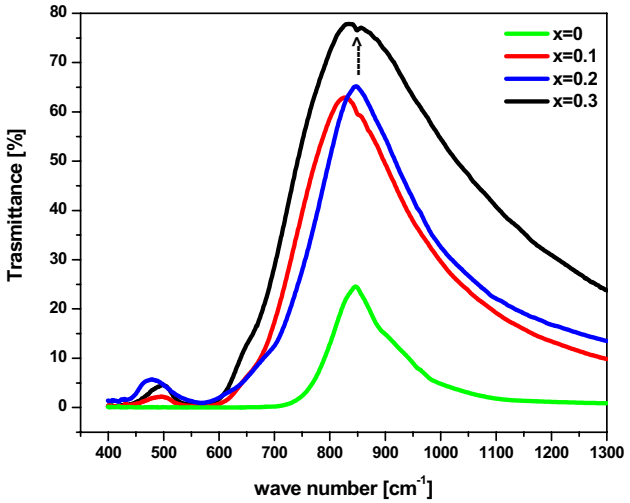

Fig. 7 IR spectra of synthesized $Co_{0.5}Cu_{0.5-x}Zn_xFe_2O_4$ ($x=0$, 0.1, 0.2, and 0.3) nano-ferrites

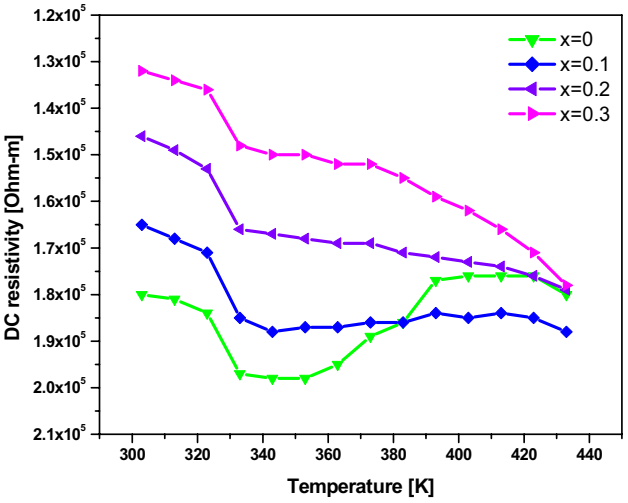

Fig. 9 Variation of DC resistivity with temperature of $Co_{0.5}Cu_{0.5-x}Zn_xFe_2O_4$ ($x=0$, 0.1, 0.2, and 0.3)

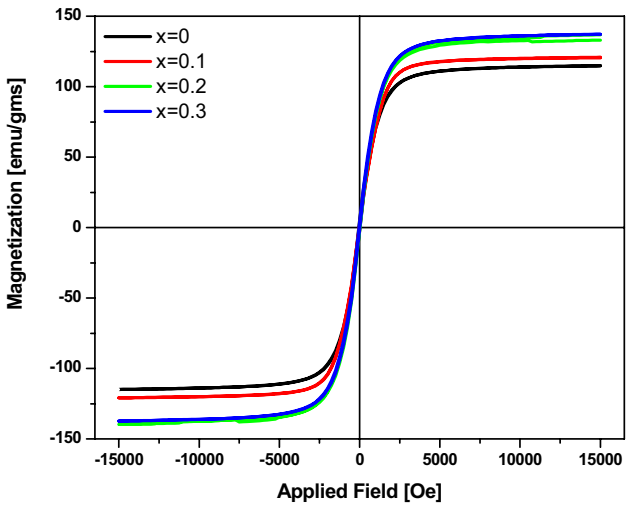

Fig. 8 Hysteresis loop for $Co_{0.5}Cu_{0.5-x}Zn_xFe_2O_4$ ($x=0$, 0.1, 0.2, and 0.3)

Table 5 Saturation magnetization, coercivity and remnant values of $Co_{0.5}Cu_{0.5-x}Zn_xFe_2O_4$ ($x=0$, 0.1, 0.2, and 0.3)

Material	Saturation magnetization (M_s) (emu/g)	Coercivity (Oe)	Remnant (emu/g)
$Co_{0.5}Cu_{0.5}Fe_2O_4$	137.246	0.223	18.141
$Co_{0.5}Cu_{0.4}Zn_{0.1}Fe_2O_4$	132.949	0.245	15.353
$Co_{0.5}Cu_{0.3}Zn_{0.2}Fe_2O_4$	120.863	0.281	14.070
$Co_{0.5}Cu_{0.2}Zn_{0.3}Fe_2O_4$	114.888	0.290	9.458

results, we can observe that only the particle size reduces, and a slight increase of the magnetization will be occurring [19]. The coercivity value of the synthesized materials increases with copper ratio owing to the porosity fall with rising dopant concentration. For obvious reasons, the coercivity is manipulated by aspects such as magneto-crystallinity, micro-strains, magnetic particle morphology, size distribution, and domain size [27].

The following explanation explains how the particular saturation magnetization of doped zinc $Co_{0.5}Cu_{0.5}Fe_2O_4$ evolved: spinel ferrites have the chemical formula $(M_{1-\delta}Fe)[MFe_{2-\delta}]O_4$, where the parentheses and square brackets denote the cation positions of tetrahedral (A) and octahedral (B) coordination, respectively. The symbol denotes the degree of inversion, which is measured as the percentage of (A) locations taken by Fe^{3+} ions. The cations in parenthesis have magnetic moment directions that are the opposite of those in square brackets. The magnetic moment of each ion for Zn^{2+}, Cu^{2+}, Co^{2+} and Fe^{3+} ions is 0 μB, 0.5 μB, 1.5 μB, and 5 μB, respectively. When the spinel $Co_{0.5}Cu_{0.5}Fe_2O_4$, the Cu^{2+} ions are partially replaced by Zn^{2+} ions, Zn^{2+} ions occupy the tetrahedral-A locations, while partial Fe^{3+} ions in the tetrahedral locations return to the octahedral-B locations. This causes an overall rise in the magnetic moment and/or specific saturation magnetization initially and then for higher [28–30].

3.8 DC resistivity

The plot has two straight-line parts, as seen in Fig. 9; hence, there are two activation energies for the two distinct regimes. The two slopes can be described by the following. When the temperature is high, the thermal energy is enough to create

vacancies and the activation energies are the total of the energies needed to generate vacancies and move electrons into them. The thermal energy is only sufficient at lower temperatures to permit the migration of electrons into vacancies that are already present in the crystal. The Neel temperature or a change in the conductivity mechanism can both affect the slope. This anomaly provides compelling evidence that magnetic ordering affects conduction. Figure shows the variation of DC resistivity of $Co_{0.5}Cu_{0.5-x}Zn_xFe_2O_4$ ($x = 0$, 0.1, 0.2, and 0.3) nano-ferrite samples measured by Wayne kerr impedance analyzer within the temperature range 308–403 K. From this study, we observed that the resistivity of each compound reduces with increasing temperature; it means that it shows the semiconducting nature of all the synthesized samples. The fall in DC resistivity with rise in temperature can be accredited to the enhancement of hopping of charge carriers between Fe^{2+} and Fe^{3+} ions that are thermally activated and also to the soaring drift mobility. De-Verwey model explicated the ferrite conduction mechanism according to which characteristic conduction in nano-ferrites is a result of the electron hopping among Fe^{2+} and Fe^{3+} ion at the B-location [31]. It is as well seen that the resistivity falls swiftly with rising temperature that ensures that the conductivity rises progressively [32–34].

The resistivity values for a specific ferrite do not vary significantly between samples. Additionally, there was no discernible change between the heating and cooling cycles for any given pellet. A number of ferrites have DC values between 10^7 and 10^9 S/ cm close to room temperature, indicating that they are effective insulators there. The figure shows the DC temperature variations for various compositions. The curves for each composition have two slopes and a single transition that are all somewhat near to the ferrites' Neel temperature. It is discovered that the values of T_N are in good agreement with those discovered theoretically by molecular field theory and experimentally using AC susceptibility tests [35, 36].

4 Conclusion

In comparison to the other three materials $Co_{0.5}Cu_{0.5-x}Zn_xFe_2O_4$ ($x = 0$, 0.1, 0.2, and 0.3), the synthesized cobalt ferrite sample had the largest mean crystallite size and the smallest lattice constant size at 1200 °C. The cubic spinel structure is confirmed by the X-ray diffraction and FTIR data. With increased Cu content, the lattice constant rises. This sample's cation distribution exhibits a normal spinel shape. The ferrites transmission bands are found to be within the expected range. The produced powders are homogeneous in shape and particle size, as evidenced in SEM pictures, although they are agglomerated to a certain extent owing to the interactions among magnetic nano-ferrites. The resistivity drops swiftly with rising temperature that ensures that the conductivity rises progressively. The coercivity is manipulated by aspects such as magneto magneto-crystallinity, micro-strains, magnetic particle morphology, size distribution, and domain size. HR-TEM and EDS data will be analyzed for future research, and also Mossbauer studies of these ferrites could be carried out as a part of future research.

Data availability Data is available on request to the corresponding author.

References

1. S. Deka, P.A. Joy, Enhanced permeability and dielectric constant of NiZn ferrite synthesized in nanocrystalline form by a combustion method. J. Am. Ceram. Soc. **90**, 1494–1499 (2007)
2. G. Ott, J. Wrba, R. Lucke, Effects of heating processing on microstructure and magnetic properties of Mn-Zn ferrites prepared via chemical co-precipitation. J. Magn. Magn. Mater. **254**, 535–537 (2003)
3. A. Nutan Gupta, S.C. Verma, D.C.D. Kashyap, Dielectric behavior of spin-deposited nanocrystalline nickel-zinc ferrite thin films processed by citrate-route. Solid State Commun. **134**, 689–694 (2005)
4. A.K. Nikumbh, R.A. Pawar, D.V. Nighot, G.S. Gugale, M.D. Sangale, M.B. Khanvilkar, A.V. Nagawade, Structural, electrical, magnetic and dielectric properties of rare-earth substituted cobalt ferrites nanoparticles synthesized by the co-precipitation method. J. Magn. Magn. Mater. **355**, 201–209 (2014)
5. T.P. Sumangala, C. Mahender, B.N. Sahu, N. Venkataramani, S. Prasad, Study of magnesium ferrite nano particles with excess iron content. Physica B **448**, 312–315 (2014)
6. L.-Z. Li, X.-X. Zhong, R. Wang, Tu. Xiao-Qiang, Structural, magnetic and electrical properties of Zr-substitued NiZnCo ferrite nanopowders. J. Magn. Magn. Mater. **435**, 58–63 (2017)
7. W. Qin, T. Nagase, Y. Umakoshi, J.A. Szpunar, Relationship between microstrain and lattice parameter change in nanocrystalline materials. Philos. Mag. Lett. **88**, 169–179 (2008)
8. N. Rezlescu, E. Rezlescu, F. Tudorache, P.D. Popa, Gas sensing properties of porous Cu Cd and Zn ferrites. Rom. Rep. Phys. **61**, 223–234 (2009)
9. S. Thankachan, B.P. Jacob, S. Xavier, E.M. Mohammed, Effect of samarium substitution on structural and magnetic properties of magnesium ferrite Nanoparticles. J. Magn. Magn. Mater. **348**, 140–145 (2013)
10. A.N. Birgani, M. Niyaifar, A. Hasanpour, Study of cation distribution of spinel zinc nano-ferrite by X-ray. J. Magn. Magn. Mater. **374**, 179–181 (2015)
11. L. Neel, C R Acad Sci Paris **230**, 375 (1950)
12. B.S. Holinsworth, N.C. Harms, S. Fan, D. Mazumdar, A. Gupta, S.A. McGill, J.L. Musfeldt, Magnetic field control of charge excitations in $CoFe_2O_4$. APL Mater. **6**, 066110 (2018)
13. Y.H. Hou, Y.J. Zhao, Z.W. Liu, H.Y. Yu, X.C. Zhong, W.Q. Qiu, D.C. Zeng, L.S. Wen, Structural, electronic and magnetic properties of partially inverse spinel $CoFe_2O_4$: a first-principles study. J. Phys. D Appl. Phys. **43**, 445003 (2010)
14. A.I. Borhan, V. Hulea, A.R. Iordan, M.N. Palamaru, Cr^{3+} and Al^{3+} co-substituted zinc ferrite: Structural analysis, magnetic and electrical properties. Polyhedron **70**, 110–118 (2014)

15. A. Pradeep, P. Priyadharsini, G. Chandrasekaran, Structural, magnetic and electrical properties of nanocrystalline zinc ferrite. J. Alloys Compd. **509**, 3917–3923 (2011)
16. M.A. Amer, T.M. Meaz, S.S. Attalah, A.I. Ghoneim, Structural and magnetic characterization of the $Mg_{0.2-x}Sr_xMn_{0.8}Fe_2O_4$ nanoparticles. J. Magn. Magn. Mater. **363**, 60–65 (2014)
17. R.K. Singh, A. Narayan, K. Prasad, R.S. Yadav, A.C. Pandey, A.K. Singh, L. Verma, R.K. Verma, Thermal, structural, magnetic and photoluminescence studies on cobalt ferrite nanoparticles obtained by citrate precursor method. J. Therm. Anal. Calorim **110**, 573–580 (2012)
18. P.P. Bardapurkar, S.S. Shewale, N.P. Barde, K.M. Jadhav, Structural, magnetic and catalytical properties of cobalt ferrite nanoparticles dispersed in silica matrix. Mater. Res. Express **6**, 045055 (2019)
19. I. Sharifi, H. Shokrollahi, Structural, Magnetic and Mössbauer evaluation of Mn substituted Co-Zn ferrite nanoparticles synthesized by co-precipitation. J. Magn. Magn. Mater. **334**, 36 (2013)
20. T.K. Pathak, N.H. Vasoya, V.K. Lakhani, K.B. Modi, Structural and magnetic phase evolution study on needle-shaped nanoparticles of magnesium ferrite. Ceram. Int. **36**, 275–281 (2010)
21. S.N. Klausen, P.A. Lindgard, K. Lefmann, F. Bodker, S. Moorup, Temperature dependence of the magnetization of disc shaped NiO nanoparticles. Phys. Status Solidi A **189**, 1039 (2002)
22. K. Jalaiah, K. Vijaya Babu, Structural, magnetic and electrical properties of nickel doped Mn-Zn spinel ferrite synthesized by sol-gel method. J. Magn. Magn. Mater. **423**, 275–280 (2017)
23. X. Huang, Y. Zhou, Wu. Wenwei, Xu. Jiawei, S. Liu, D. Liu, Wu. Juan, Effect of Zn^{2+} substitution on the structure and magnetic properties of $Co_{0.5}Cu_{0.5}Fe_2O_4$ synthesized by solvothermal method. J. Electron. Mater. **45**, 3113–3120 (2016)
24. G. Satyanarayana, G. Nageswara Rao, K. Vijaya Babu, G.V. Santosh Kumar, G. Dinesh Reddy, Effect of Cr^{3+} substitution on the structural, electrical and magnetic properties of $Ni_{0.7}Zn_{0.2}Cu_{0.1}Fe_{2-x}Cr_xO_4$ ferrites. J. Korean Phys. Soc. **74**, 684–694 (2019)
25. M.M.N. Ansari, S. Khan, N. Ahmad, Influence of Dy^{3+} and Cu substitution on the structural, electrical and dielectric properties of $CoFe_2O_4$ nanoferrites. J. Mater. Sci. Mater. Electron. **30**, 17630–17642 (2019)
26. N.H. Vasoya, V.K. Lakhani, P.U. Sharma, K.B. Modi, R. Kumar, H.H. Joshi, Study on the electrical and dielectric behaviour of Zn-substituted cobalt ferrialuminates. J. Phys. Condens. Matter. **18**, 8063 (2006)
27. D.R. Mane, D. Birajdar, S. Patil, S.E. Shirsath, Redistribution of cations and enhancement in magnetic properties of sol-gel synthesized $Cu_{0.7-x}Co_xZn_{0.3}Fe_2O_4$ ($0 \leq x \leq 0.5$). J. Sol-Gel. Sci. Technol. **58**, 70–79 (2011)
28. G. Vinod, K. Rajashekhar, Y. Sandeep, J.L. Naik, Influence of RE-Gd^{3+} ion substitution on structure, morphology, optical, and magnetic analysis of Cu-Cd based nano ferrites synthesized by low-temperature citrate sol-gel auto combustion method. J. Magn. Magn. Mater. **562**, 169772–169778 (2022)
29. M. Mostafa, O. Saleh, A.M. Henaish, S.A. Abd El-Karem, R. Ghazy, O.M. Hemeda, A.M. Dorgham, H. Al-Ghamdi, A.H. Almuqrin, M.I. Sayyed, S.V. Trukhanov, E.L. Trukhanova, A.V. Trukhanov, D. Zhou, M.A. Darwish, Structure morphology and electrical/magnetic properties of Ni-Mg nano-ferrites from a new perspective. Nanomaterials **1045**, 1–28 (2022)
30. K. Pal, A. Si, G.S. El-Sayyad, M.A. Elkodous, R. Kumar, A.I. El-Batal, S. Kralj, S. Thomas, Cutting edge development on graphene derivatives modified by liquid crystal and CdS/TiO2 hybrid matrix: optoelectronics and biotechnological aspects. Crit. Rev. Solid State Mater. Sci. **46**, 385–449 (2021)
31. A. Sandeep, G. Ganesh, S. Swathi, N. Rajesh, M. Sreelatha, P.K.N. Kumari, B. Brahmanandam, S.C. Bose Rapaka, D. Ravinder, J. Shanker, P.K. Naini, Synthesis, structural, magnetic and optical studies of Eu doped Ni-Zn nano ferrites. Ceram. Int. **48**, 29493–29501 (2002)
32. B.L. Shinde, U.M. Mandle, A.M. Pachpinde, K.S. Lohar, Synthesis and characterization of Al^{3+} substituted Ni-Cu-Zn nano ferrites. J. Therm. Anal. Calorim **147**, 2947–2956 (2022)
33. M.A. Elkodous, G.S. El-Sayyad, A.E. Mohamed, K. Pal, N. Asthana, F.G. de Souza Junior, F.M. Mosallam, M. Gobara, A.I. El-Batal, Layer-by-layer preparation and characterization of recyclable nanocomposite (CoxNi1-xFe2O4; x = 0.9/SiO2/TiO2). J. Mater. Sci. Mater Electron. **30**, 8312–8328 (2019)
34. S. Sagadevan, K. Pal, Z.Z. Chowdhury, M.E. Hoque, Structural, optical and dielectric investigation of $CdFe_2O_4$ nanoparticles. Mater. Res. Expres **4**, 075025 (2017)
35. K. Pal, A.A.A. Aljabali, S. Kralj, S. Thomas, F.G. de Souza, Graphene-assembly liquid crystalline and nanopolymer hybridization: a review on switchable device implementations. Chemosphere **263**, 128104 (2021)
36. D.R. Kumar, C.A. Lincoln, G.V. Charan, G. Thara, D. Ravinder, M. Veeraswamy, P. Naresh, Study of photo catalytical, antimicrobial activity, dielectric and ac impedance properties of Zn doped Mg nanoferrites synthesized from citrate gel auto combustion method. J. Mat. Chem. Phys. **278**, 125648 (2022)

Authors and Affiliations

B. Trinadh[1,2] · J. Suresh[3,7] · A. Rama Krishna[4,7] · K. Vijaya Babu[5] · B. Vikram Babu[6,7] · P. V. S. S. S. N. Reddy[8] · B. Sathish Mohan[9] · K. Samatha[1]

[1] Department of Physics, Andhra University, Visakhapatnam 530003, India

[2] G. V. S. M. Govt. Degree College, SPSR Nellore, Ulavapadu, AP 523292, India

[3] Department of Physics, BVC College of Engineering, Palacharla, Rajamahendravaram, AP 533102, India

[4] Department of ECE, Aditya College of Engineering and Technology, Surampalem, India

[5] Department of Physics, Centurion University of Technology and Management, Vizianagaram 535003, India

[6] Department of Physics, International School of Technology and Sciences (ISTS) for Women, Rajanagaram, Rajamahendravaram, Andhra Pradesh 533294, India

[7] Jawaharlal Nehru Technological University Kakinada (JNTUK), Kakinada, AP 533003, India

[8] Department of Physics, Government Degree College, Ravulapalem, AP 533238, India

[9] Bio Enviro Chemical Solutions, Visakhapatnam 530017, India